LNF-98/031

The Beamline SINBAD at DAΦNE

A. Marcelli, E. Burattini, A. Nucara, P. Calvani, G. Cinque, C. Mencuccini, S. Lupi,
F. Monti, M. Sanchez Del Rio

Il Nuovo Cimento 20 D, 4, 463–481, (1998)
Paper written for the 3rd Workshop on "Development of Infrared Syncrhrotron Radiation and Applications to Materials Science", Orsay, 27–28 March 1997.

IL NUOVO CIMENTO VOL. 20 D, N. 4 Aprile 1998

The beamline SINBAD at DAΦNE(*)

A. MARCELLI(1), E. BURATTINI(1)(2), A. NUCARA(3), P. CALVANI(3), G. CINQUE(2)
C. MENCUCCINI(1)(4), S. LUPI(3), F. MONTI(2) and M. SANCHEZ DEL RIO(5)

(1) *Laboratori Nazionali INFN di Frascati, C.P. 13 - 00044 Frascati, Italy*
(2) *Facoltà di Scienze, Università di Verona - 37134 Verona, Italy*
(3) *Dipartimento di Fisica, Università di Roma I "La Sapienza" and INFM - 00185 Roma, Italy*
(4) *Dipartimento di Energetica, Università di Roma I "La Sapienza" - 00185 Roma, Italy*
(5) *ESRF - BP 220, 38043 Grenoble Cedex, France*

(ricevuto il 21 Novembre 1997; approvato il 7 Gennaio 1998)

Summary. — SINBAD, the first beamline in Italy designed to work in the far- and mid-infrared region, is being installed on DAΦNE storage ring, the new Φ-factory at *Laboratori Nazionali di Frascati*. DAΦNE, first injected in September 1997, will work at 0.51 GeV with a beam current in the range 2–5 A. The infrared synchrotron radiation extracted from a bending magnet is expected to be more brilliant than a black body at 2000 K up to three orders of magnitude in the wavelength range 10-1000 μm. The optical layout of SINBAD, fully designed by ray tracing simulation, includes six mirrors placed in a 18 m long beamline. The infrared radiation is first focused on a wedged diamond window and then re-focused on the entrance of a Michelson interferometer. Diffraction effects and mirror roughness, as well as optical aberrations, have been evaluated.

PACS 42.72 – Optical sources and standards.
PACS 01.30.Cc – Conference proceedings.

1. – Introduction

The natural divergence of synchrotron radiation (SR) grows with the wavelength and may become as large as several tenths of mrads in the infrared range (IRSR): nevertheless, SR remains much more brilliant than thermal sources in the mid-, far-IR range, except for lasers. Those, including tunable FELs, cannot compete with IRSR in most spectroscopic applications due to the much broader spectrum of synchrotron emission.

(*) Paper written for the 3rd Workshop on "Development of Infrared Synchrotron Radiation and Applications to Materials Science", Orsay, 27-28 March 1997.

The unique characteristics of IRSR were already pointed out in 1973 by Stevenson *et al.* [1]. Three years later, Lagarde and Meyer [2] reported the first experimental observation of IRSR at LURE, Orsay, and in 1984 Yarwood *et al.* [3] used the SRS ring of Daresbury as a very powerful IR source. IR beamlines for a variety of experiments were then installed on UVSOR at Okazaki, on NSLS at Brookhaven, and on BESSY in Berlin. Today, several IRSR facilities are available in the world, most of which collect radiation from bending magnets; a beamline at LURE, Orsay, collecting the radiation emitted by an undulator [4] is in operation, while an apparatus in Madison [5] exploits the *edge* radiation [6]. Another beamline based on this principle is projected in Karlsruhe [7].

The present contribution describes the optical layout and the calculated performances of SINBAD (Synchrotron INfrared Beamline At DAΦNE). This beamline is designed and optimised to work in the wavelength range from 5 to 5000 μm. It will also be possible to work at shorter wavelengths, although with reduced performances.

The scheme of the article is the following. The basic concept of SINBAD is illustrated in sect. **2**, while the parameters and characteristics of the DAΦNE ring and of its IRSR emission are described in sect. **3**. Section **4** is dedicated to the beamline design, on the base of ray tracing calculations. Therein the two sections of the beamline are described in detail: the ultra-high vacuum part where the divergent radiation emitted by the bending magnet is focused on a wedged diamond window, and the high-vacuum part that transmits the radiation from the window to the interferometer. The expected performances in terms of transmission and polarisation properties are summarised in sect. **5**, while the brilliance gain at the sample position, obtained by ray tracing the optical scheme of the Michelson interferometer, is discussed in sect. **6**.

2. – Why an infrared beamline on DAΦNE?

DAΦNE (Double Annular Φ-factory for Nice Experiments) is the electron-positron collider realized at Laboratori Nazionali INFN of Frascati, where the first beam was injected at the end of September, 1997. This double ring is designed to work at an energy of 0.51 GeV per beam to produce Φ-mesons by electron-positron annihilation. Due to this low-energy value, the emitted radiation will be characterised by a low critical energy ϵ_c (see table I). However, this will not affect the intensity of the infrared emission, because in this energy region the emission is independent of E. The natural emittance of DAΦNE ($\sim 10^{-6}$ m rad) is higher than a "third generation" SR source. This parameter may be not so relevant in the IR region where one has to face a considerable divergence of the SR beam itself. On the other hand, DAΦNE will be a very powerful IR source thanks to the high beam current I (from 2 A at commissioning up to 5 A, when working in a topping up mode) [8]. Such a high current will result in a brilliance gain of two or three orders of magnitude for SINBAD, with respect to far-infrared conventional sources [9, 10].

Due to the reduced X-ray emission, which extends up to roughly 5 KeV for a DAΦNE bending magnet (ϵ_c=208 eV), the use of a low-energy ring seems suitable for IRSR applications. So, the power load on the first optical element (the extraction mirror) is quite low. On the contrary, third-generation rings are characterized by a higher electron energy E and a much lower emittance, resulting in power densities as large as several W/mm^2, which represent severe constraints to the optical system.

TABLE I. – *The* DAΦNE *storage ring parameters.* ϵ_c *is the critical energy.*

Energy	510 MeV	$(\gamma = E/mc^2 = 10^3)$
Dipole bending radius	1.4 m	
Dipole magnetic field	1.2 T	
Dipole critical energy	ϵ_c=208 eV	
Wiggler bending radius	0.94 m	
Wiggler magnetic field	1.8 T	
Wiggler critical energy	ϵ_c=311 eV	
Wiggler period length	0.64 m	$N_{\text{period}} = 3$
Coupling coefficient k	0.01	
Energy loss/turn electron	9.3 keV	
Natural horizontal emittance	10^{-6} mrad	
Natural bunch length σ_z	0.81 cm	
Anomalous bunch length σ_z	3.0 cm	
Bunch separation	4.2 m	
Number of particles/bunch	$9 \cdot 10^{10}$	
Number of bunches	1–120	
Maximum total average current	5.3 A	
RF frequency	368.25 MHz	
Maximum SR Power/beam	49 kW	
Total single beam lifetime	<3 h	

3. – DAΦNE as an infrared radiation source

The DAΦNE layout consists of a system of accelerators including an electron-positron linac, a damping ring and two separated rings for e^+ and e^- collision experiments. Its whole design is based on conventional technology. The collider inside the experimental hall is shown in fig. 1. The storage rings, crossing in the horizontal plane, consist of two symmetric parts with similar structure: an inner one named *short* and an outer one named *long*. The collider includes two interaction regions where two large apparata for particle detection will be installed. The two rings will be characterised by the same magnetic structure as well as the same optical functions [11]. The photon beam will be extracted from the *long* external arc section, both from a wiggler and from a bending magnet (BM) [8]. Table I reports the main parameters of the DAΦNE project [11-14].

The first figure of merit is the ratio of IRSR brilliance to the corresponding quantity for a black body. The brilliance is defined as the photon flux normalized to the solid angle and to the source dimensions. For a SR source, the number of photons emitted in a solid angle $\mathrm{d}\theta\,\mathrm{d}\psi$ and in a bandwidth $\frac{\delta\lambda}{\lambda} = 0.1\%$ is related to the beam current I and to the electron energy E by the equation [15]

$$(1) \qquad \frac{\mathrm{d}^2 F}{\mathrm{d}\theta\,\mathrm{d}\psi} = 1.327 \times 10^{19} E^2 I \left(\frac{\lambda_c}{\lambda}\right)^2 K_{2/3}^2 \left(\frac{\lambda_c}{2\lambda}\right) \qquad (\text{photons/mrad}^2/\text{sec}),$$

where λ_c is the critical wavelength for the DAΦNE magnet and K is a modified Bessel function. The source size depends on the machine parameters, the SR wavelength λ and both the horizontal and vertical collection angles. We can introduce the Actual Source Area (ASA) as an effective area of the SR source that takes into account the different broadening phenomena and describes the extended source.

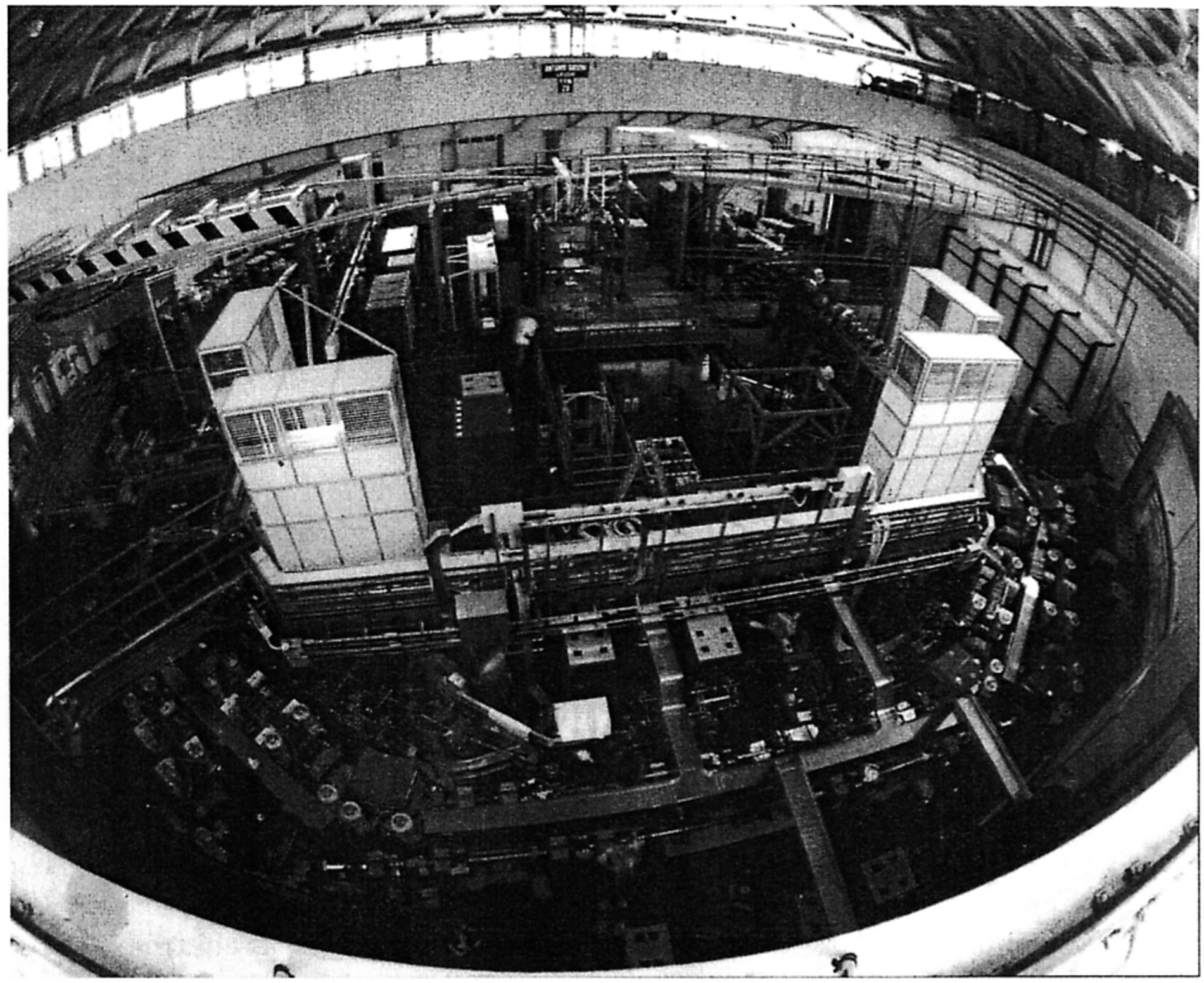

Fig. 1. – The DAΦNE main rings assembled in the experimental hall.

In the IR range, the ASA can be evaluated using the relation [9]

$$2\pi\Sigma_x\Sigma_y = 2\pi\sqrt{\sigma_x^2 + \sigma_r^2 + (\sigma_x^{\mathrm{geom}})^2}\sqrt{\sigma_y^2 + \sigma_r^2 + (\sigma_y^{\mathrm{geom}})^2} \qquad (\mathrm{cm}^2), \tag{2}$$

where Σ_x and Σ_y are, respectively, the r.m.s. values of the horizontal and vertical dimensions of the source and σ_x and σ_y represent the horizontal and the vertical contributions, due both to the electron beam size and to the optical functions of the ring [9]. The diffraction-limited source size σ_r is related to the intrinsic divergence of the radiation σ_ψ through

$$\sigma_r(\lambda) = \left(\frac{\lambda}{4\pi\sigma_\psi}\right) \qquad (\mathrm{cm}). \tag{3}$$

In the infrared region ($\lambda \gg \lambda_c$) [16]

$$\sigma_\psi(\lambda) = 0.816\left(\frac{\lambda}{\lambda_c}\right)^{0.354}\frac{10^{-3}}{E} \qquad (\mathrm{rad}). \tag{4}$$

The geometrical terms $\sigma_i{}^{\mathrm{geom}}$ in eq. (2) represent the projection of the source arc of length l on the xy plane intersecting the arc length at its mid-point, which is assumed to

TABLE II. – *The* DAΦNE *sources, including the diffraction term* (*see* eq. (2)) *and for* $\theta = 20$ mrad.

λ (μm)	Σ_x (mm)	Σ_y (mm)
10	2.12	0.32
100	2.18	0.35
1000	2.28	0.76

be the virtual location of the extended source. In other words, these terms are due to the finite length of the electron trajectory usually observed along the bending magnet; the electron bunch along the trajectory is approximated as a uniform distribution [9]. When the SR is collected under small angles, the geometrical terms are usually negligible. This is not the case of IRSR, because of the simultaneous effect of a large intrinsic divergence σ_ψ and of a large collecting angle θ. When θ increases, the SR source becomes an arc of length $l = 2\theta\rho$, where ρ is the radius of the BM.

From eqs. (2), (3) and (4) the source dimensions can be calculated for any λ. Using the parameters of the bending magnet and a horizontal angle of 20 mrad, we obtained the values reported in table II.

The SR brilliance can now be defined as

$$B_{\mathrm{SR}} = \frac{\frac{\mathrm{d}^2 F}{\mathrm{d}\theta\,\mathrm{d}\psi}}{\mathrm{ASA}} \qquad (\mathrm{photons/0.1\%bw/sec/mrad^2/cm^2}). \tag{5}$$

On the other hand, the brilliance B_{BB} of a black-body source can be derived from the well-known Planck's law for the power density

$$n_{\mathrm{BB}} = \frac{2c10^{-3}}{\lambda^3 \left(e^{\frac{hc}{k_B T \lambda}} - 1\right)} S\Omega \qquad (\mathrm{photons/0.1\%bw/sec}), \tag{6}$$

where S and Ω are the emitting surface and solid angle, respectively.

The actual brilliance ratio of the SR source to the black body, as evaluated from eqs. (5) and (6) with T=2000 K and S=0.45 cm^2 [9, 10], is shown in fig. 2a) for different values of the collecting angle, ranging from 5 to 100 mrad. A gain of several orders of magnitude over a black-body source is obtainable by using the synchrotron radiation of DAΦNE in the whole infrared region. Anyway, good performances at all wavelengths are obtained when the collecting angle is about 20 mrad. For comparison, a similar calculation performed for the NSLS light source at Brookhaven is shown in fig. 2b). The lower emittance of the Brookhaven ring allows to get a slightly higher gain only in the near IR region.

The source dimensions reported in table II are used as inputs for the ray tracing simulations. These are based on SHADOW [17], a powerful code that takes into account both the machine parameters, *i.e.* emittance and energy, and the geometrical dimensions of the source at fixed wavelength in a defined bandwidth. The code output is a distribution of rays (5000 in the present simulation) in a given region of space created using the Monte Carlo technique to sample the spatial, angular and spectral distributions of the source (here, a bending magnet). Each ray is fully described by four vectors and two phases: the starting position $\vec{r}$, the wavevector $\vec{k}$, the electric vectors $\vec{A}_{\mathrm{s}}$, and $\vec{A}_{\mathrm{p}}$ and their associated phases ϕ_{s} and ϕ_{p}. Once the optical layout is defined, the source is traced through

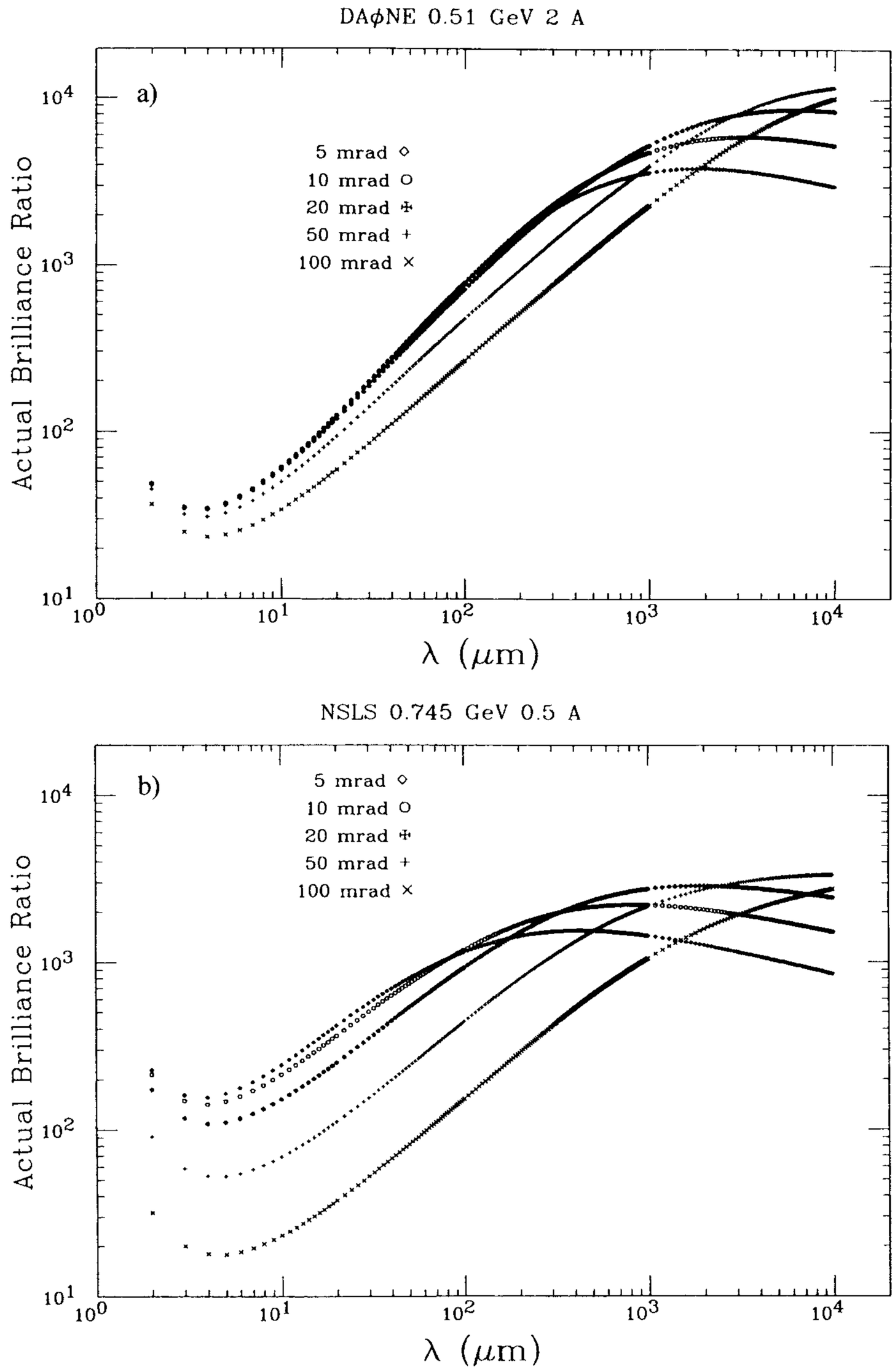

Fig. 2. – a) The ABR function of the DAΦNE source, as calculated for different values of the collecting angle θ; b) the ABR calculated in the same way for the NSLS ring at Brookhaven is reported for comparison.

the elements of the optical system, *i.e.* mirrors, windows, crystals of a variety of shapes, taking into account also optical imperfections. As SHADOW is a ray tracing code, it calculates the geometrical broadening and the beam size but not the diffraction effect. Since these contributions to the total size are not negligible in the IR domain, the data reported in table II include, via eq. (2), *ad hoc* corrections for the diffractive contribution as from eq. (3). The results of the source simulation are reported in fig. 3, while the distribution parameters are reported in table III.

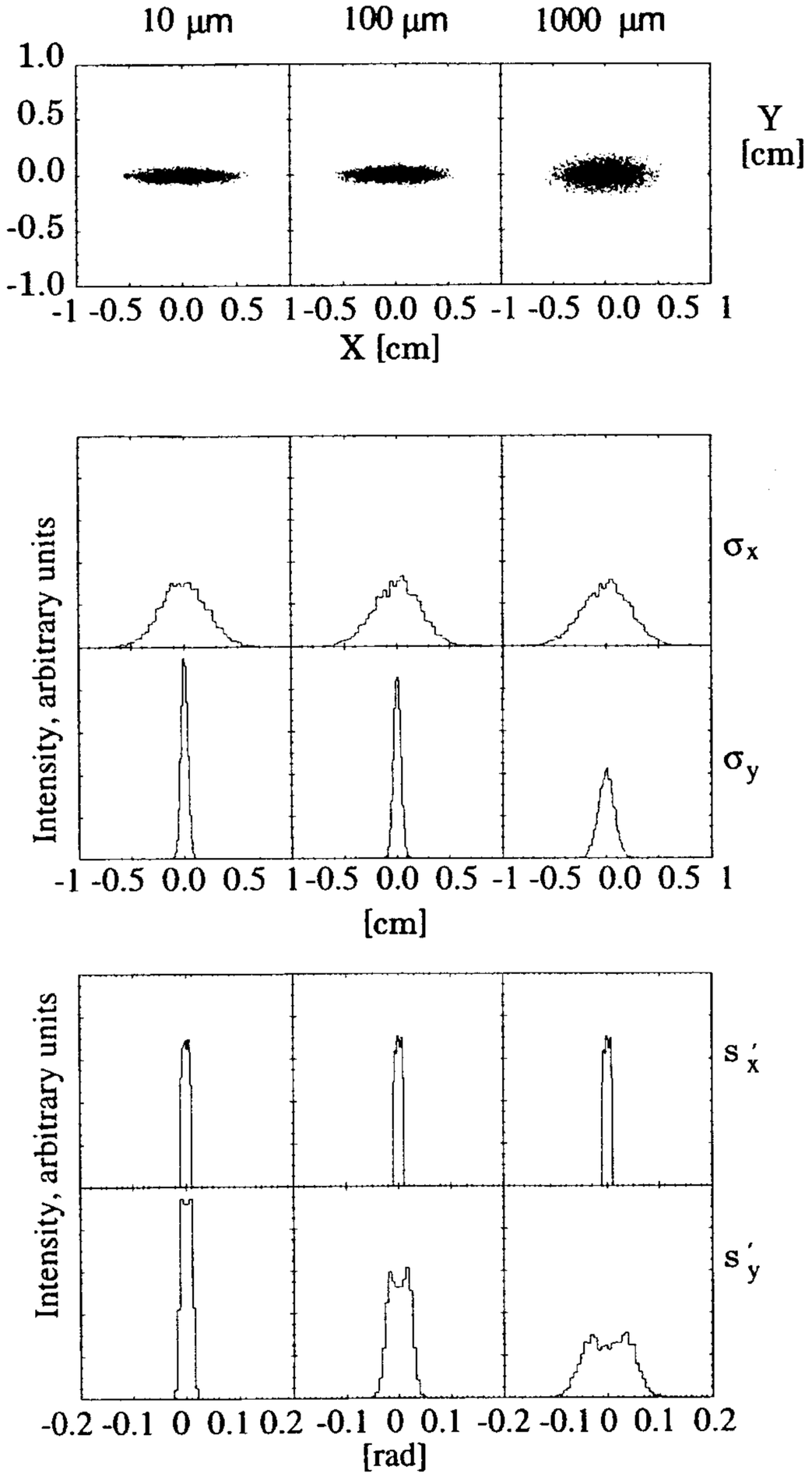

Fig. 3. – From left to right: plots of the source generated by SHADOW at 10 μm, 100 μm and 1000 μm. From top to bottom: distributions of the emitted intensity in the (x, y)-plane, the spatial distributions in the vertical (y) and horizontal plane (x) and the angular distribution s'_x (fixed to 20 mrad) and s'_y.

TABLE III. – *Output parameters of the ray tracing code for the sources shown in fig.* 3. s'_x *and* s'_y *are the width at half maximum of the non-Gaussian distributions.*

λ (μm)	σ_x (cm)	σ_y (cm)	s'_x (rad)	s'_y (rad)
10	0.210	0.33	0.0058	0.010
100	0.216	0.46	0.0058	0.019
1000	0.226	0.81	0.0058	0.040

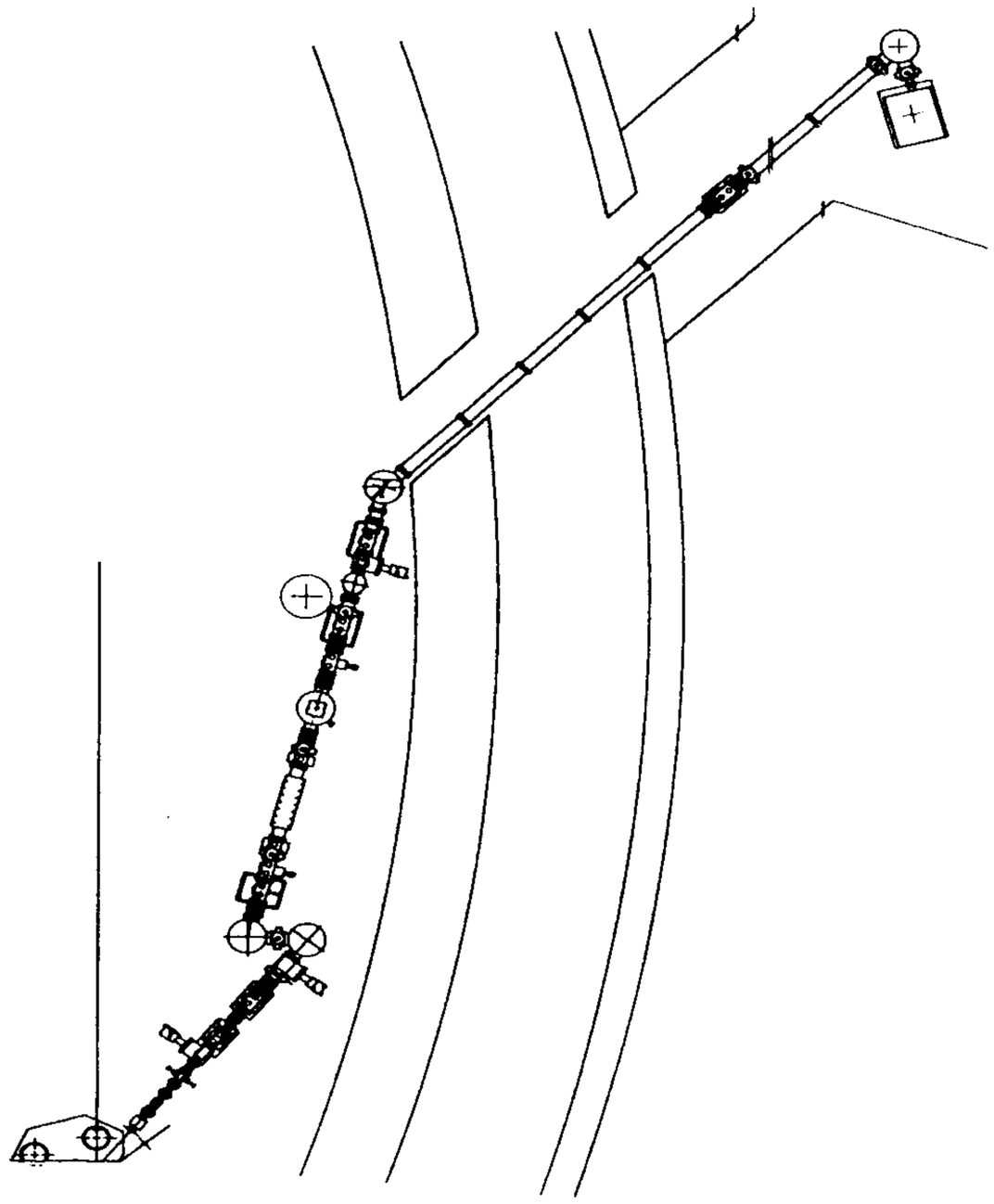

Fig. 4. – Top view of the SINBAD beamline layout.

The solid angle of the IR port at DAΦNE is limited by the geometrical constraint of the front-end flange (CF 4 $\frac{1}{2}$ inches) placed at 1.2 m from the centre of the source. Both in the horizontal and in the vertical plane, the clear aperture is roughly 50 mrad. However, in our simulations the horizontal collection angle has been set to 20 mrad and the optical elements have been dimensioned to accept such smaller divergence. This reduction does not yield significant effects at short wavelengths ($\lambda < 200$ μm), while it causes an intensity damping at higher wavelengths [10]. Although this choice may appear as limiting, it is the best to optimise the IRSR emission both in the mid and in the far IR range. Indeed, as demonstrated by fig. 2, the large horizontal size of the DAΦNE source obtainable by increasing the horizontal collection angle produces only a reduction of the brilliance [9,10].

4. – The SINBAD design

Following the first optical simulations of the preliminary layouts considered [18], several additional constraints were included. Anyway, the main problem to solve remains the matching of the large and variable divergence of the SR in the IR domain to the interferometer f number. As the divergence grows with the wavelength and becomes larger than 100 mrad in the far IR, it is impossible to transfer the radiation to the interferometer placed at about 20 m from the source, unless the radiation is focused along its path.

The final design of the system, shown in fig. 4, is the best compromise in order to obtain the highest throughput, reduced aberrations, stability of the spot image, optical manufacturing feasibility, and cost. The first straight part of the beamline is the front-end discussed in the next section. After that, the photon beam is deflected in the horizontal plane by an extraction plane mirror and then focussed on the diamond window (DW) by an ellipsoidal mirror with a demagnification 2:1. The DW separates the final part of the

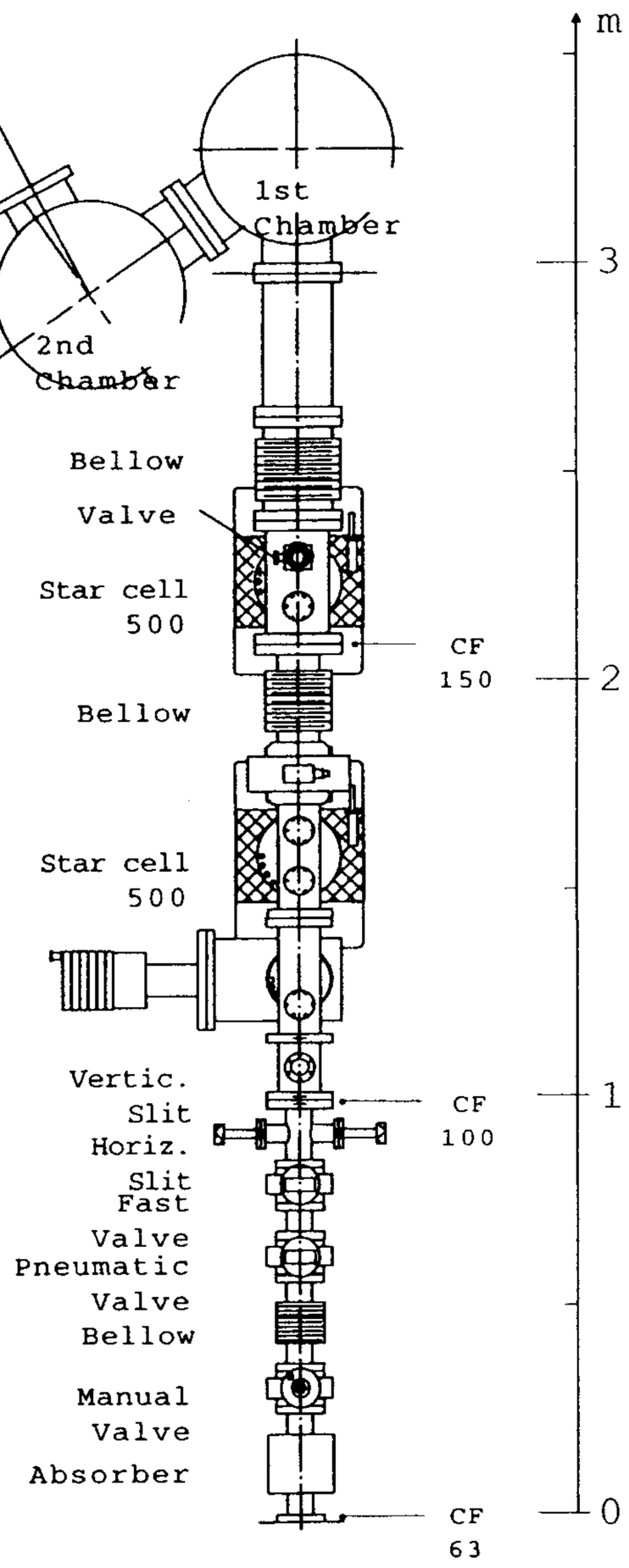

Fig. 5. – Top view of the front-end elements.

beamline, closest to the storage ring and working in a ultra-high vacuum (UHV), from the final part nearest to the experimental apparatus which normally works under high vacuum conditions. Such high vacuum conditions (HV) allow to reduce absorption of the radiation by the residual gas in the long pipe of SINBAD.

After the DW the beam diverges again: then a toroidal mirror together with a plane one deflect the radiation in the vertical plane, collimate the beam in both planes and lift it by 50 cm. A plane mirror, placed before the shielding wall of the storage ring hall, deflects the radiation into a tunnel towards the experimental area, where the last optical element of SINBAD (a toroidal mirror) focuses the radiation on the entrance pupil of the interferometer.

4·1. *The front-end and the ultra-high-vacuum section of* SINBAD. – The first section of the beamline, directly connected to the storage ring, is kept under UHV (10^{-10} Torr). The front-end, shown in top view in fig. 5, is mainly designed to protect the storage ring when the beamline is operating. Since the viewport opened in the storage ring vacuum chamber is 120 cm far from the SR source, and considering that the SINBAD front-end is

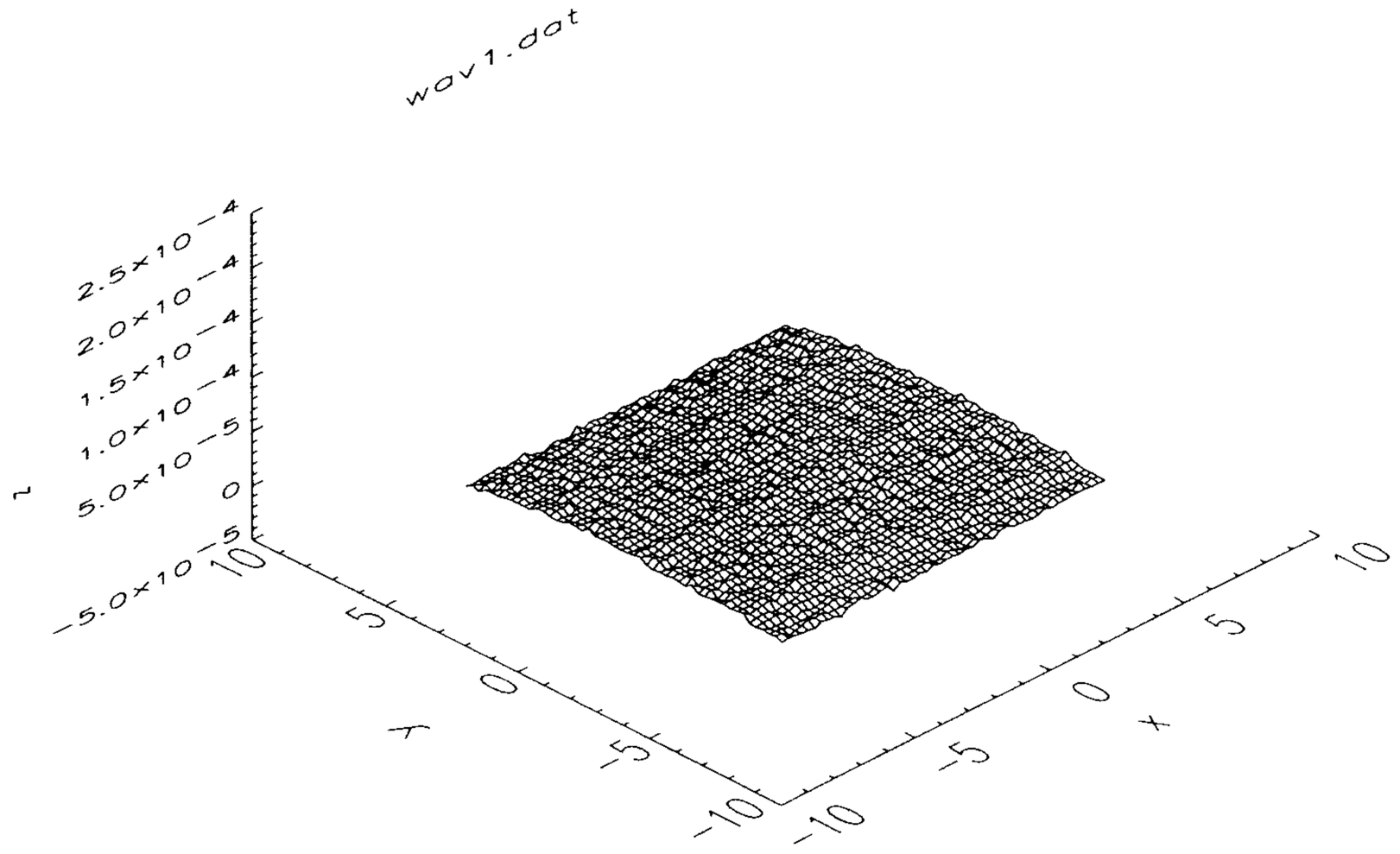

Fig. 6. – Simulated waviness of the optical surface of the mirror M1 with 5 arcsec slope error.

about 3 m long, the extraction mirror (M1) is finally placed at about 4.5 m from the source. M1 is made of OFHC copper, gold coated, with three internal cooling channels to reduce the effects of thermal load. It deflects the SR beam by an angle of 55° in the horizontal plane towards an ellipsoidal mirror (M2), whose semi-axes are 379 cm and 269 cm, placed 70 cm downstream. The incidence angle on M2 is 40°. The DW is placed on the second focus of the ellipsoid, and the spot at DW represents, for all the other optical elements, the effective source traced to the entrance pupil of the interferometer. The quality of the spot is strongly dependent on the accuracy of the aspherical surface of M2. Once the mirror parameters are fixed, the quality of the reflecting surface is affected both by the roughness and by the slope error. In the IR domain, the request on the roughness is not so severe, while the slope error contribution has to be carefully considered. In order to predict the behavior of the SINBAD mirrors, we have generated *virtual* surfaces with variable slope errors Δ both in the sagittal and in the tangential planes according to the method described in [19]. Tests on the beam size in the focus of the ellipsoid at different wavelengths indicate that the divergence in the sagittal direction is unaffected by any reasonable value of the surface irregularity, while an increase of the divergence at short wavelengths is observed for a slope error of about 10 arcsec in the tangential plane. As a consequence, the mirrors of SINBAD are designed to fulfill the specifications for a slope error of less than 5 arcsec in the incidence plane and less than 50 arcsec in the sagittal one. A typical simulated surface with a defined slope error for the ray tracing simulations is shown in fig. 6 [19].

Ray tracing simulations allowed also to evaluate the influence of mechanical errors in the angular orientations of the optical elements, the effects of aberrations induced by any deviation from the ideal position of the aspherical elements, and the distortion of the mirrors induced by thermal load. For SINBAD, as the estimated power density is $Q = 8$ W/cm^2, we calculated for the first Cu mirror a deformation with a slope Δ=0.43 mrad. This value corresponds to a radius of curvature of R=581 m that, at λ=50 μm, should induce a broadening of the original spot on the DW by 0.23 mm in the vertical direction. Due to the spot size and the large divergence of the IR radiation, the effects of thermal bump on the final brilliance is practically negligible [20].

4·2. *The diamond window.* – One of the most important elements of the beamline design is the diamond window, a 124° wedged ~800 μm thick chemical vapour deposition self-substained diamond film (CVDD) with a diameter of 15 mm, brazed on a double-sided CF flange. Usually natural diamond crystals [4, 21], KRS-5 or silicon [22] are employed for this purpose. These last two solutions, however, do not allow the transmission of the entire IR range nor of the visible part of the spectrum, useful for the optical alignement. To preserve the possibility of transmitting the visible and all the IR range, we have considered for SINBAD the use of thin CVDD films, which also represent a low-cost solution. Diamond does not absorb radiation in the whole optical domain except for a narrow range in the mid infrared and it is the hardest known material. Moreover, its thermal conductivity, higher than that of copper by a factor of 4, ensures good heat dissipation. With respect to natural diamond, CVDD films obtained by chemical vapor deposition exhibit very similar optical properties [23] at a much lower cost. The hardness of CVDD material is also very high (>7000 Knoops), so that a pressure difference of 1 atm can be safely sustained.

Before making our choice, we tested several CVDD films with a minimum thickness of 250 μm, both plane and wedged, supplied by General Electric of USA and DRUKKER of Holland. The wedged windows were preferred in order to reduce the interference of the multiple reflections typically observed in plane windows at wavelengths comparable to their thickness [23]. Collected data have shown that the interference phenomena are substantially suppressed and the residual noise is less than 5%. Due to unpolarised contributions coming from the off-plane IRSR emission, we expect that a wedged window is more effective in suppressing interferences than a flat window mounted at the Brewster angle [21].

The image of the source created by the ellipsoid on the CVDD window is shown in fig. 7 for different wavelengths. Notice that the expected aberrations at this stage are negligible.

Diffraction effects from an angular aperture smaller than the intrinsic IRSR divergence are not taken into account in the adopted simulation. In fact, since the IRSR divergence is much smaller than that of a black body both in the near and mid IR, these effects may be neglected. On the contrary, at wavelengths of the order of 1000 μm, due to the increase of the SR natural divergence, a blur of the image is expected, as shown in fig. 7, due to the presence of the front-end flange which limits the vertical acceptance to 50 mrad. Although the diffraction-limited size is introduced in the description of the source (see eq. (3) in sect. 3) the above diffraction effect from a geometrical aperture cannot be simulated with the procedure here employed.

4·3. *The high-vacuum section of* SINBAD. – The second section of the beamline connects the DW to the interferometer and is kept under high-vacuum conditions in order to minimize absorption by the residual gas. It is designed to transfer the new source, *i.e.* the image produced by the ellipsoidal mirror on the DW, to the entrance pupil of the interferometer.

Several constraints due to the existing building, like the shielding walls, the size and position of their apertures and the level of the ground in the laboratory area affected the design of this section. Several optical layouts were figured out and simulated by ray-tracing. The different performances were evaluated [24] taking into account the transmittance of the beamline and the spot size and divergence. According to ray tracing simulations, if only the optical performances are considered, the best solution is to transfer the beam as a plane wave both in the horizontal and in the vertical plane and refocuse it on the pupil of the interferometer using 4 off-axis paraboloids [24]: two placed just after

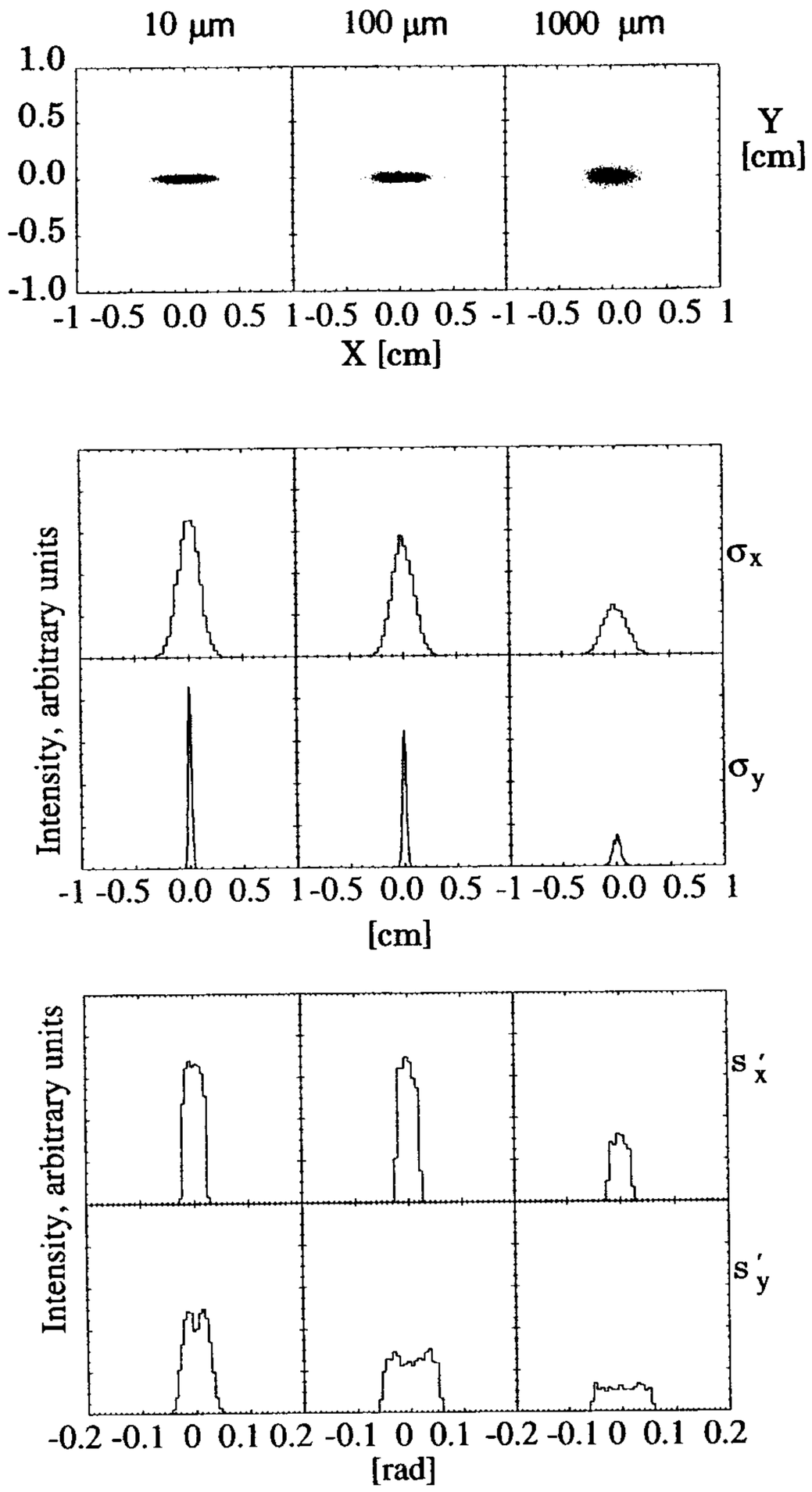

Fig. 7. – From left to right: the image on the diamond window at 10 μm, 100 μm and 1000 μm, as simulated by SHADOW. From top to bottom: distributions of the emitted intensity in the (x, y)-plane, spatial distributions in the vertical (y) and horizontal plane (x) and angular distributions s'_x and s'_y.

the DW and the other two before the interferometer.

For the sake of design flexibility and taking into account the cost of the optical elements, a layout including two plane mirrors and two toroids was finally chosen (see table IV and fig. 8). The first mirror (M3) of the second section, 80 cm far from the DW (the new effective source), is toroidal and deflects vertically the radiation by 90°. The second mirror (M4) is plane and also deflects the radiation by 90°, so that the outcoming beam is parallel to the incoming on M3 but vertically shifted by 50 cm. The third mirror (M5) is also plane and deflects the beam horizontally into the tunnel towards the experimental area. The final toroidal mirror (M6) is placed at the end of the transfer line to deflect the radiation by 60° and focuse it at 0.5 m from its pole.

By this layout the SR beam is transferred both vertically and horizontally as a plane

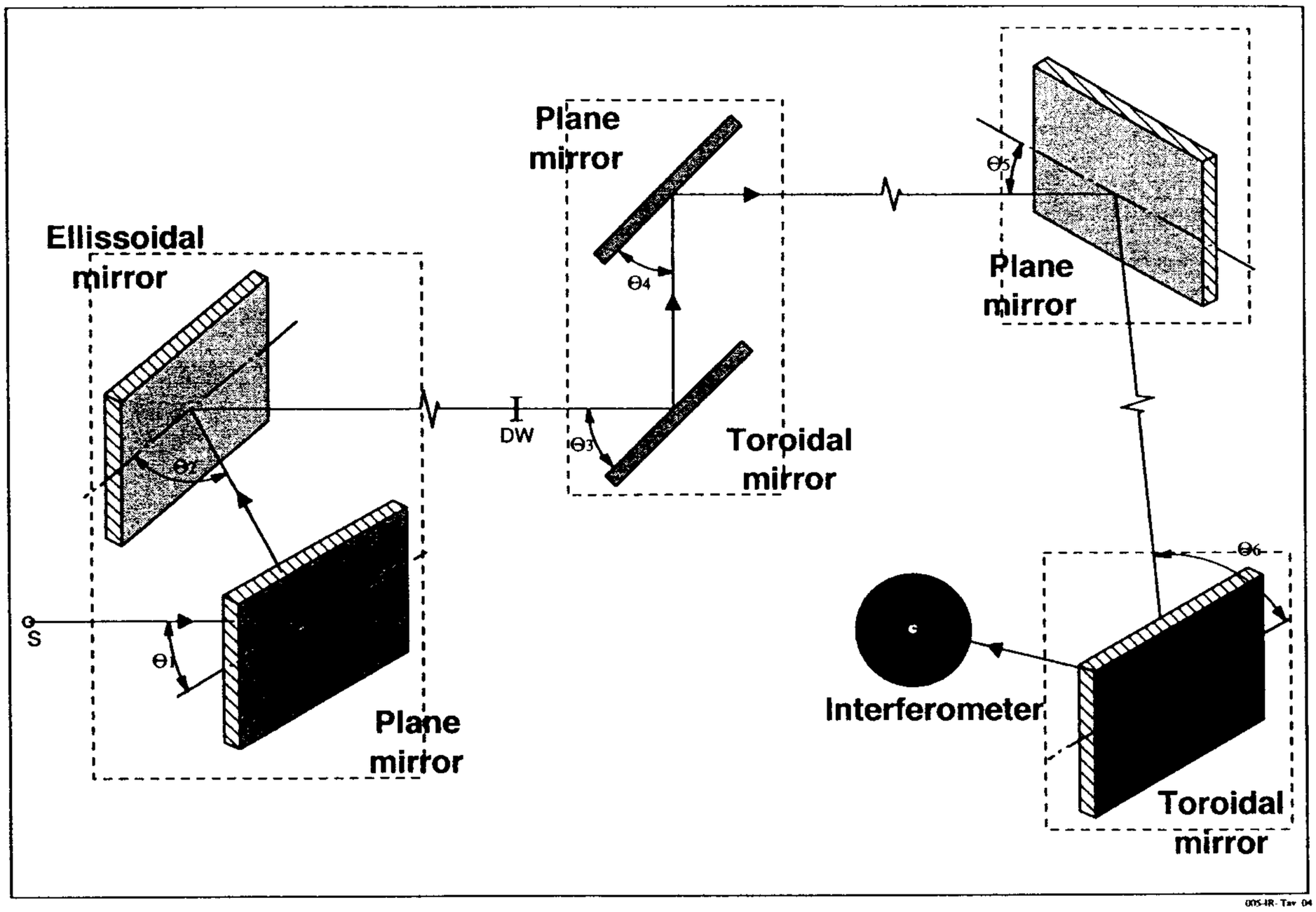

Fig. 8. – Optical layout of the SINBAD beamline. The divergent beam is focused on DW by the ellipsoid (M2). The first toroidal mirror (M3) transforms the divergent beam in an almost parallel fan, that is refocused at the end of the path by the second toroid (M6). M1, M4 and M5 are plane mirrors.

wave, and the final spot is well focused: however, due to the use of toroidal mirrors, geometrical aberrations may be clearly observed. In fig. 9, the spots produced at 100 μm and at 1000 μm by a beamline with 4 parabolic off-axis mirrors are compared with those obtained by replacing the aspherical mirrors with two planes and two toroids, *i.e.* with the final optical layout of SINBAD. Figure 9 clearly shows the presence of aberrations due to the use of toroids: nevertheless, the spot size is practically identical for both the optical configurations. The simulation also shows that the first toroidal mirror (M3) does not introduce any strong aberration, but the residual divergence of the beam after the re-

TABLE IV. – *Parameters of the* SINBAD *mirrors. The distance is measured from the previous optical element. For* M2 *the last two columns report the semi-major and semi-minor axes.*

	Distance (cm)	Incidence angle	Figure	Major radius (cm)	Minor radius (cm)
M1	–	27.5°	plane		
M2	70	40°	ellipsoidal	379	269
M3	80	45°	toroidal	226	113
M4	50	45°	plane		
M5	312	72.5°	plane		
M6	1300	30°	toroidal	116	87

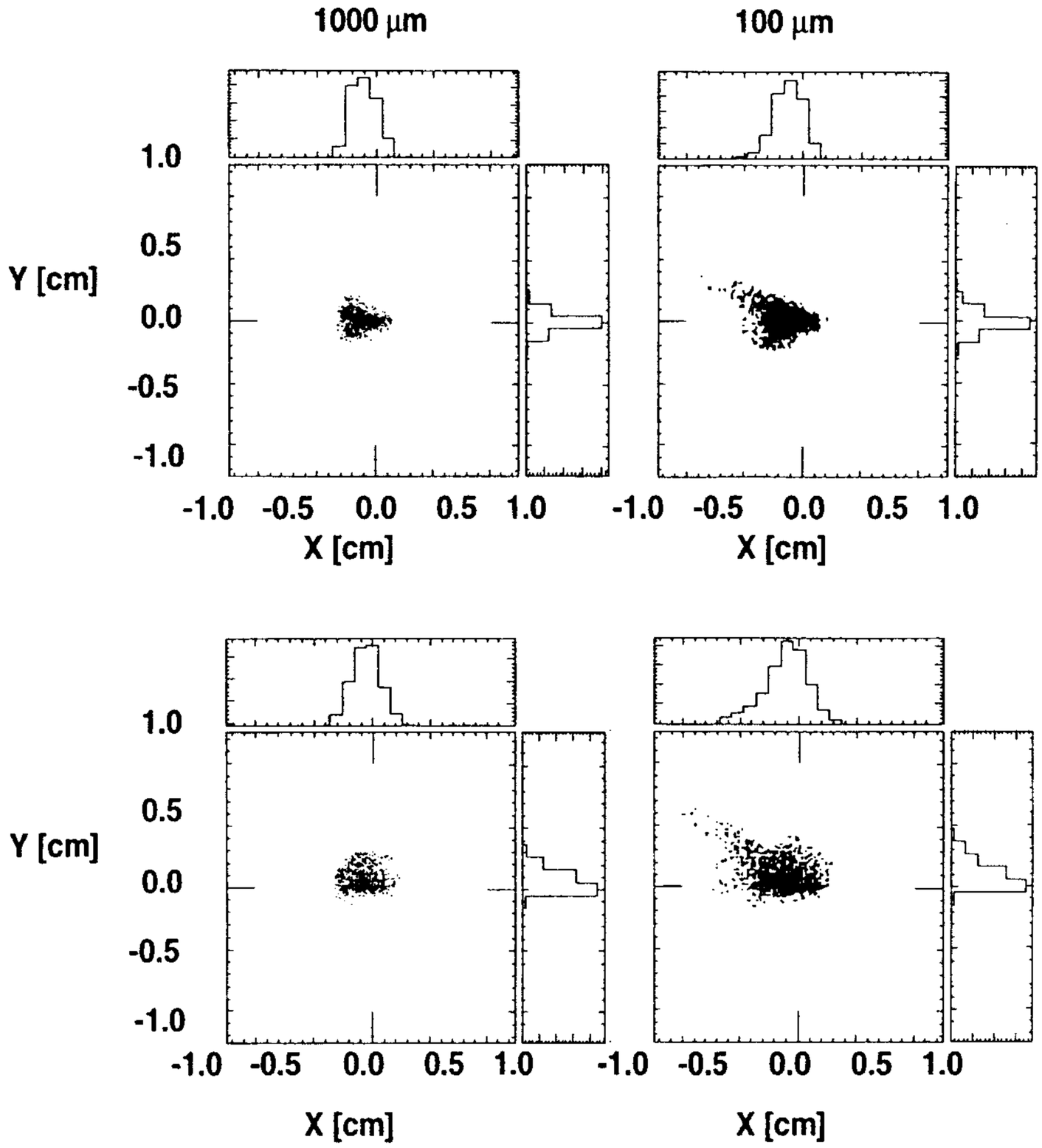

Fig. 9. – Spots obtained at 100 and 1000 μm by the same optical layout with M3 and M4 given by two off-axis paraboloids (top panels) and M3 and M4 given by a toroid and a plane mirror, respectively (bottom panels).

flection generates a wave front which is not perfectly plane. The aberrations produced by the second toroid (M6) are stronger. Its short focal length, due to the existing laboratory constraints, is responsible for the observed broadening of the final image (coma), even if the demagnification of the beamline is almost equal to one in both planes. To summarize, the obtained results are fully satisfactory in comparison with those of much more complex layouts including a larger number of mirrors [24].

5. – The SINBAD performances

In order to improve the accuracy of the ray-tracing simulations, we have also taken into account the finite reflectivity of gold coating and the slope errors of the six mirror surfaces. The resulting properties of the SINBAD optical scheme appears quite satisfactory, finally yielding a small, round and intense infrared spot. Different final images are reported in fig. 10 while the corresponding data are summarised in table V. As already discussed and shown in fig. 7, the diffraction effects due to the apertures placed along the line, that could eventually affect the source images in the region of millimetric wavelengths, are not considered in fig. 9 and fig. 10.

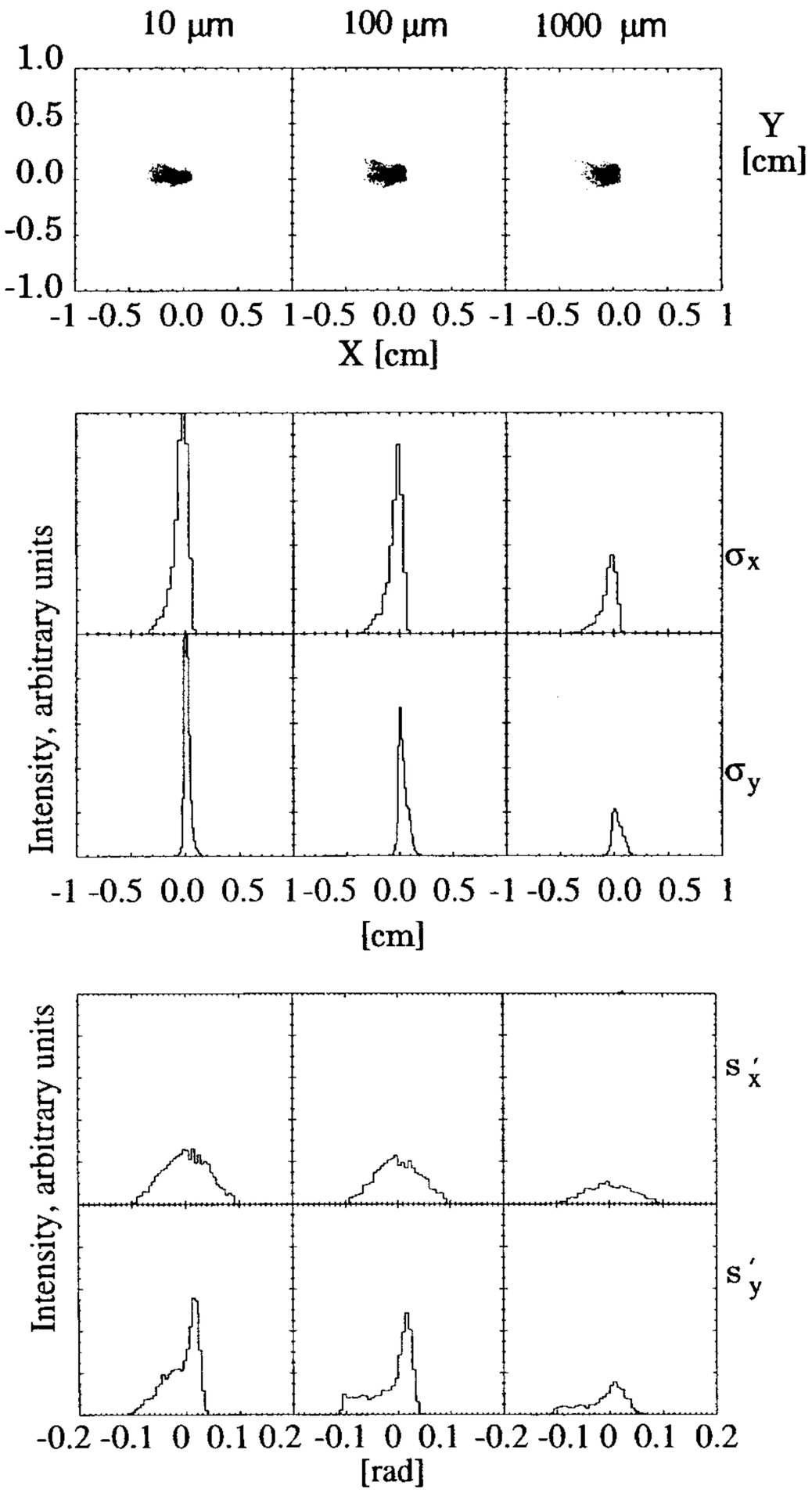

Fig. 10. – From left to right, plots of the final image obtained by the optical system of table IV at 10 μm, 100 μm and 1000 μm. From top to bottom: distributions of the emitted intensity in the (x, y)-plane, the spatial distributions in the vertical (y) and horizontal plane (x) and the angular distributions s'_x and s'_y.

The data in table V confirm a still high transmittance of the system at large wavelengths, and give the divergence of the radiation at the entrance of the instrument. Knowing the interferometer f-number, it is possible to calculate both the effective photon flux and the brilliance at the sample position (see sect. **6**).

5˙**1**. *Degree of polarisation.* – It is well known that SR is linearly polarised in the orbital plane, while above and below it is elliptically polarized. When observed at a particular angle over the orbit, the radiation is circularly polarized. Since the early pioneering works in the visible region [25], several investigations performed both in the VUV and X-ray region fully confirmed these predictions.

In order to investigate the degree of circular polarisation of SR from DAΦNE in the

TABLE V. – *Standard deviations for the images shown in fig.* 10. *The angle s'_y is the width at half maximum of the non-Gaussian distributions. In the last column T is the estimated transmission.*

λ (μm)	σ_x (cm)	σ_y (cm)	σ'_x (rad)	s'_y (rad)	T (%)
10	0.07	0.048	0.036	0.097	>99
100	0.07	0.072	0.037	0.136	83
1000	0.07	0.053	0.039	0.152	38

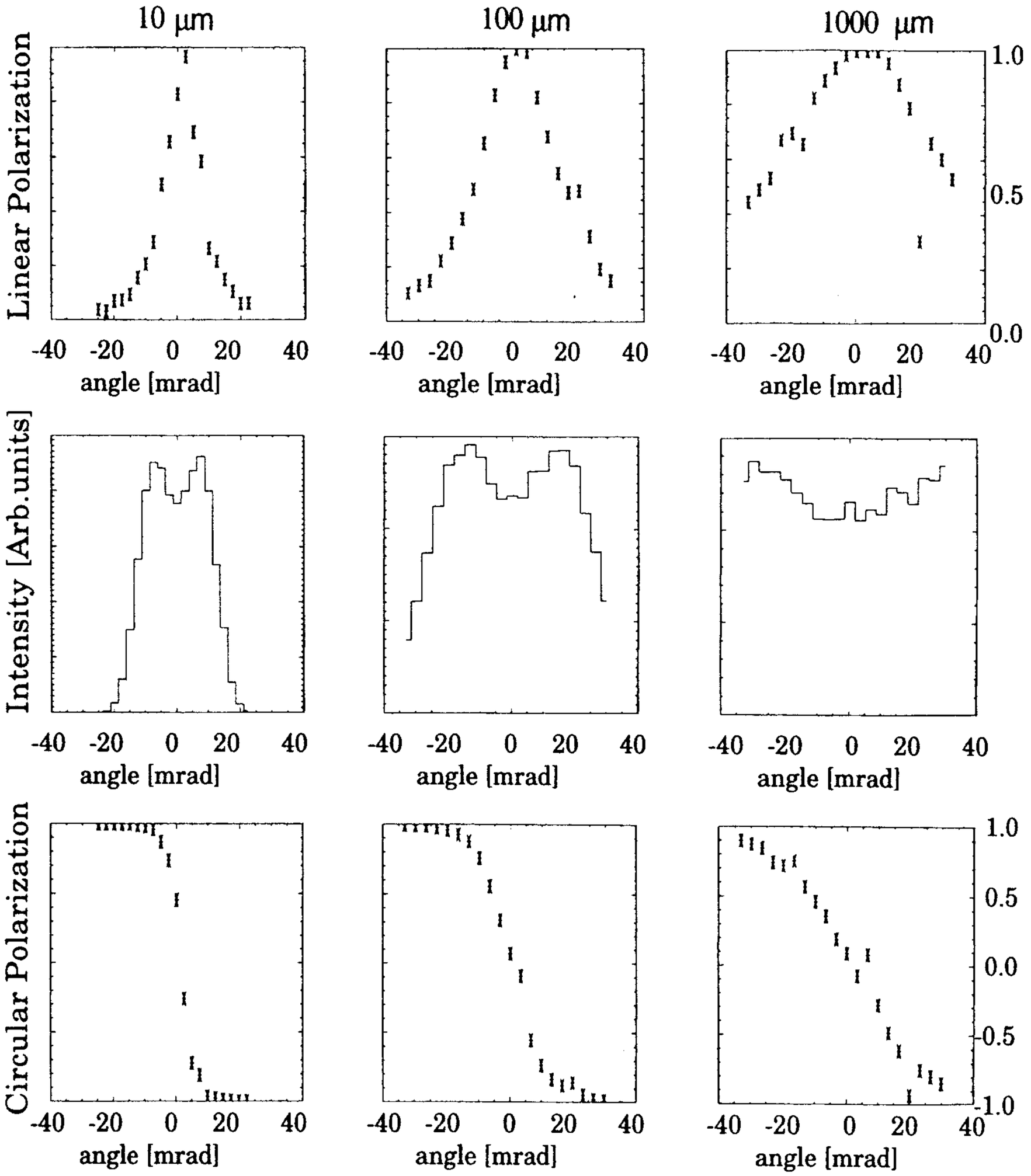

Fig. 11. – In the central panels from left to right at increasing λ, the photon flux through a slit 4 mm wide, and placed out of the orbital plane. In the top and bottom panels the corresponding linear and circular degrees of polarisation.

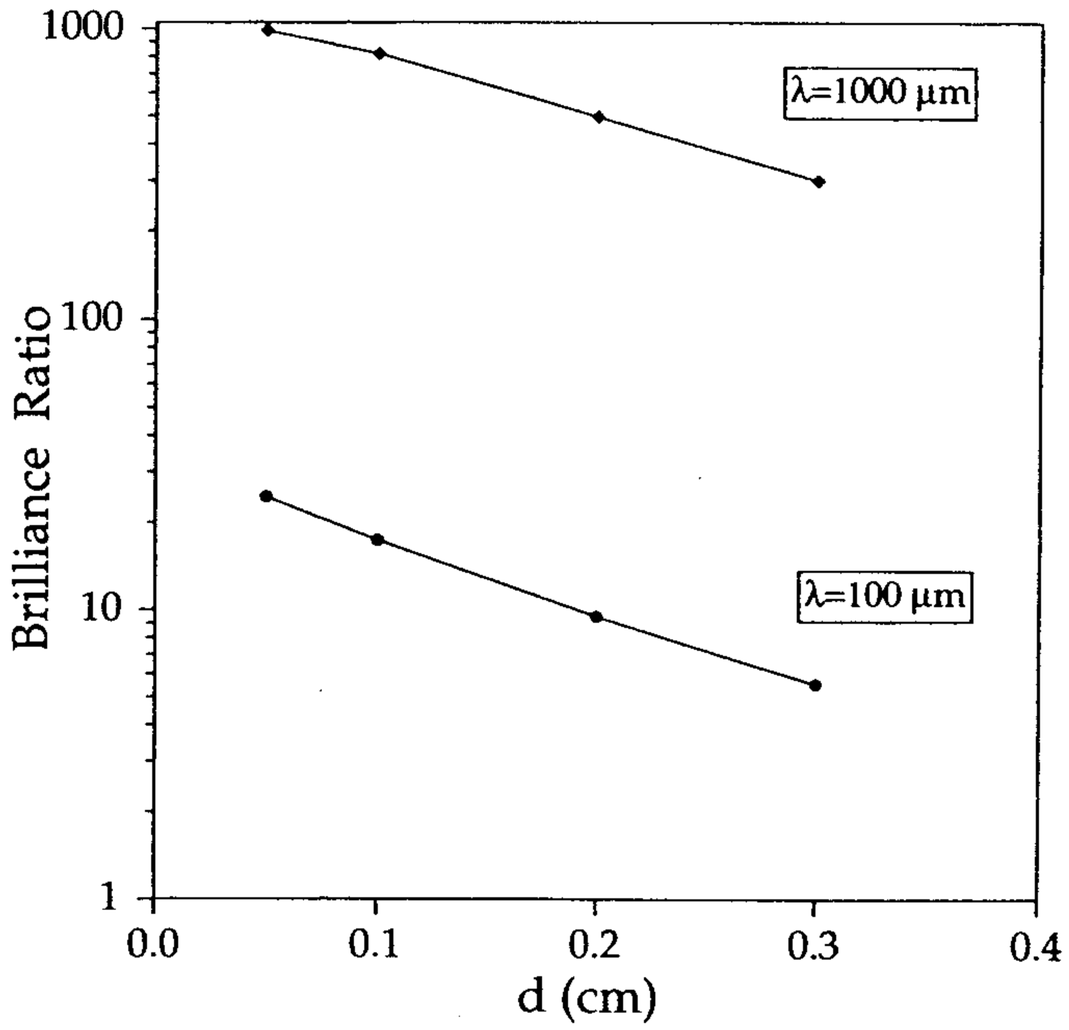

Fig. 12. – Brilliance gain at the sample position (see text) for two different wavelengths and different aperture diameters d.

IR domain, the code SHADOW has also been applied to the optics of SINBAD.

Simulating a narrow slit (4 mm in aperture) placed at variable height above the orbital plane, we analysed the characteristics of the source both after the slit and at the end of the beamline. In order to have good statistics, we increased the standard number of traced rays up to 20000.

This simulation indicates that the slit selects a fraction between 5% and 10% of the total flux, depending on the radiation frequency and the azimuthal angle. The degree of circular polarisation at the source is almost equal to 1.

At the end of the beamline, the final results shown in fig. 11 demonstrate that a slit intercepting 5% of the total flux and placed at an azimutal angle of 15 mrad above the optical system transmits to the interferometer a degree of circular polarisation larger than 80%.

6. – The brilliance available for the experiment

In sect. 3 we report the ABR function, *i.e.* the gain in brilliance of the DAΦNE IRSR source in comparison with a black body. For the purpouse of the experiment, it is more useful to know the brilliance gain at the sample position, *i.e.* at the end of the beamline including the interferometer optics, in our case a BRUKER suitably modified to work under vacuum. The interferometer has also been included in the SHADOW simulation. The black body used as reference (subscript BB) is simulated by a Gaussian source (σ=0.25 cm) and seen under a collection angle Ω=0.09 srad. The calculations were performed at two wavelengths: λ=100 μm and λ=1000 μm. Moreover, we considered several circular apertures of different diameters d ranging from 0.05 cm up to 0.3 cm at the focal point (sample compartment in the interferometer) in order to estimated the brilliance

ratio (BR). This is given by

$$\mathrm{BR} = \frac{N^d_{\mathrm{SR}}}{N^d_{\mathrm{BB}}} \frac{N_{\mathrm{BB}}}{N_{\mathrm{SR}}} \frac{n_{\mathrm{SR}}}{n_{\mathrm{BB}}}, \tag{7}$$

where, N^d_{SR} and N^d_{BB} are the number of rays passing through a given aperture for the synchrotron and the blackbody source, respectively; N_{SR} and N_{BB} are the initial number of rays, and n_{SR}, n_{BB} are the number of photons emitted by the two sources: n_{BB} can be derived from eq. (6), while the number n_{SR} of the photons emitted by our bending magnet can be obtained from the general expression of the SR emission curve [26-28].

The behaviour of the different spot sizes on the sample at the two previous wavelengths is reported in fig. 12. Therein, we introduced the highest limit for the BB emission and neglected the multiple reflections along the optical path of the beamline. As a consequence, the gain shown in fig. 12 is considerably underestimated.

* * *

The authors wish to thank H. BUYS, G. CAPPUCCIO, R. S. SUSSMANN and G.P. WILLIAMS for useful discussions and technical suggestions. A special thank is devoted to D. CANNAVÒ, G. CIBIN, A. GRILLI, A. RACO and S. SIMEONI for their continuous support in the design phase of this challenging system. This work has been partially supported by the EC HC&M contract 94-0551 project.

REFERENCES

[1] STEVENSON J. R., ELLIS H. and BARTLETT R., *Appl. Opt.*, **12** (1973) 2884.
[2] MEYER P. and LAGARDE P., *J. Phys.*, **37** (1976) 1387.
[3] YARWOOD J., SHUTTLEWORTH T., HASTED J. B. and NANBA T.,, *Nature*, **312** (1984) 742.
[4] ROY P., MATHIS Y.-L., GERSCHEL A., MAEX J.-P., MICHAUT J., LAGARDE B. and CALVANI P., *Nucl. Instrum. Methods A*, **325** (1993) 568.
[5] BOSCH R. A., *Nuovo Cimento D*, this issue, p. 483.
[6] BOSCH R. A., MAY T. E., REININGER R. and GREEN M. A., *Rev. Sci. Instrum.*, **67** (1996).
[7] MATHIS Y.-L., ROY P., NUCARA A., LUPI S., TREMBLAY B., CALVANI P. and GERSCHEL A., preprint.
[8] MARCELLI A. and CALVANI P., LNF Report 93/027 (IR), 1993.
[9] NUCARA A., CALVANI P., MARCELLI A. and SANCHEZ DEL RIO M., LNF Report 94/053 (IR), 1994.
[10] NUCARA A., CALVANI P., MARCELLI A. and SANCHEZ DEL RIO M., *Rev. Sci. Instrum.*, **66** (1995) 1934.
[11] BASSETTI M., BIAGINI M. E., BISCARI C., GUIDUCCI S., MASULLO M. R. and VIGNOLA G., DAΦNE Technical Note L-1, 1991.
[12] BIAGINI M. E., GUIDUCCI S., MASULLO M. R. and VIGNOLA G., DAΦNE Technical Note L-4, 1991.
[13] DAΦNE Machine Project, LNF-92/033 (P), 1992.
[14] LEE-FRANZINI J., LNF-94/077 (P), 1994.
[15] HULBERT S. L. and WEBER J. M., *Nucl. Instrum. Methods A*, **319** (1992) 25.
[16] X Ray Data Booklet, Center for X-ray optics, Lawrence Berkeley Laboratory, University of California, 1986.
[17] WELNAK C., CHEN G. J. and CERRINA F., *Nucl. Instrum. Methods A*, **347** (1994) 344.
[18] BURATTINI E., CAPPUCCIO G., MARCELLI A., CALVANI C., NUCARA A. and SANCHEZ DEL RIO M., *Nucl. Instrum. Methods A*, **347** (1994) 308.
[19] SANCHEZ DEL RIO M. and MARCELLI A., *Nucl. Instrum. Methods A*, **319** (1992) 170.

[20] SMITHER R. K., *Nucl. Instrum. Methods A*, **291** (1990) 286.
[21] SLATER D. A., HOLLINS P., CHESTERS M. A., PRITCHARD J., MARTIN D. H., SURMAN M., SHAW D. A. and MUNRO I. H., *Rev. Sci. Instrum.*, **63** (1992) 1547.
[22] NELANDER B., *Vibrat. Spectrosc.*, **9** (1995) 29.
[23] SUSSMANN R. S., PICKLES C. S. J., BRANDON J. R., WORT C. J. H., DODGE C. N., BEALE A. C., KREHAN A. J., DORE P., NUCARA A. and CALVANI P., this issue, p. 503.
[24] AMBROGINI R., Thesis, University La Sapienza, Roma, 1997.
[25] ADO YU. M. and CHERENKOV P. A., *Sov. Phys. Dokl.*, **1** (1957) 517.
[26] MARCELLI A., BURATTINI E., MENCUCCINI C., NUCARA A., CALVANI P., LUPI S. and SANCHEZ DEL RIO M., *International Symposium on Optical Science, Engineering, and Instrumentation, SPIE* Vol. **3153**, San Diego, 1997, p. 21.
[27] MARCELLI A., BURATTINI E., MENCUCCINI C., CALVANI P., NUCARA A., LUPI S. and SANCHEZ DEL RIO M., to be published in *J. Synchr. Radiat.*
[28] GREEN K., *Spectra and Optics of Synchrotron Radiation*, BNL-50522, 1976.